RESEARCH ARTICLE

# Finite element study of lumbar spine model implanted with transverse process pedicle screw fixation system

Hongwei Zhang*

School of Mechanics and Architecture, Jinan University, Guangzhou, Guangdong, China.

**Received:** November 5, 2024; **accepted:** March 11, 2025.

**Traditional pedicle screws are mostly made of metal and are used in spinal surgery. Its main surgical uses include fixation of spinal fractures, correction of spinal deformities, and spinal fusion surgery. However, the accuracy of traditional vertebral arch screws is difficult to guarantee, and they are prone to stress shielding leading to bone resorption, as well as postoperative complications such as infection, loosening or breakage of internal fixation. This study focused on modeling and analyzing a transverse process-pedicle screw (TPPS) fixation system as an alternative to conventional pedicle screws. A refined lumbar spine model was developed and a finite element model integrating TPPS with the lumbar spine was created. This study mainly used finite element method and software to simulate and verify the feasibility and effectiveness of TPPS, providing theoretical basis for surgery. The transverse process steel plate of TPPS showed good anchoring force for the transverse process in the lumbar spine. Compared with traditional pedicle screws, it had a special anchoring method, which could better serve lumbar spine surgery and prevent pedicle screw detachment. Conducting finite element research on TPPS filled the gap of no mechanical finite element research on TPPS, providing a mechanical theoretical basis for physicians to perform corrective surgeries using TPPS.**

**Keywords:** transverse process-pedicle screw fixation system; lumbar spine structure; finite element model; biomechanics.

***Corresponding author:** Hongwei Zhang, School of Mechanics and Architecture, Jinan University, Guangzhou 510632, Guangdong, China. Email: top3623@163.com.

## Introduction

The lumbar spine, a crucial part of the human body, has seen a rise in patients with lumbar spine diseases due to technological advancements in society [1, 2]. Many of these conditions necessitate lumbar corrective surgery. Traditional procedures using conventional pedicle screws often face challenges and are prone to loosening postoperatively [3-5]. There are currently several critical issues in the application of pedicle screws for spinal orthopedic surgery. Traditional pedicle screws have issues like weak anchoring, stress concentration, and suboptimal fusion. Biomechanical studies have been done to optimize implantation for reduced stress. Presently, adapting to individual differences, ensuring long-term stability, and improving biocompatibility are pressing concerns. With the global aging population, spinal disease rates, especially osteoporotic fractures, are rising. This heightens the demand for high performance pedicle screws and the need for better fixation and long-term stability. As spinal surgery advances from simple decompression to complex reconstruction and correction, pedicle screws must meet more intricate demands like providing precise support and stable fixation in three-dimensional (3D) spinal correction. To combat screw loosening, bone cement-augmented pedicle screws have been developed, providing stronger anchoring within the vertebrae [6, 7]. However, the use of bone cement poses a risk of leakage during and after surgery, potentially harming the patient. Consequently, there is a continuous quest for improved corrective surgery techniques.

Finite element analysis (FEA) offers a cost-effective method to simulate and analyze various corrective procedures, aiding in the development of optimal surgical plans [8-10]. Unlike animal experiments, FEA can accurately assess interactions within the human lumbar spine [11, 12], measure stress levels and range of motion (ROM) at specific sites, and ensure reproducibility [13]. Biomechanical studies on the lumbar spine have a long history [14, 15]. Yamamoto *et al*. conducted *in vitro* experiments in 1989 to understand spinal mobility under different conditions, which laid the foundation for finite element research in biomechanics [16]. In biomechanical research, due to the challenges faced by experiments with real models such as difficulties in sample acquisition, high costs, and the inability to precisely control experimental conditions, finite element models are needed as substitutes to optimize the design of medical devices such as pedicle screws, as well as to study disease mechanisms and predict surgical outcomes, which are not only crucial tools for biomechanical theoretical research but also important bridges connecting basic research and clinical applications. In practical applications, finite element models can be used in the research and development of medical devices and also assist in formulating personalized medical treatment plans by constructing personalized models. The currently developed finite element models of lumbar spine are relatively rough with insufficient details. Many models do not establish soft tissues such as ligaments, annulus fibrosus, and nucleus pulposus, which have a significant impact on mechanical analysis. In 1994, Shirazi-Adl developed a finite element model for the first through fifth lumbar vertebrae, focusing on axial compression, flexion, lateral bending, extension, and axial torsion [17]. While this model provided a certain level of accuracy in simulating multi-segment lumbar motion systems and became a reference for researchers, it did not achieve the precision of real models due to technical constraints. Other scientists developed a finite element model of the L3-S1 lumbar spine and validated it using male Computed Tomography (CT) images and experimental data from the literature. However, it did not address specific lumbar surgeries [18, 19]. Lin *et al*. established a finite element model for the L1-L5 lumbar spine to investigate the effects of dynamic spine stabilizers based on CT images from a 19-year-old healthy male and validated against experimental data from previous studies [20]. While this study represented a significant advancement in surgical biomechanics, the finite element model used was relatively coarse compared to actual lumbar models. In terms of model construction, the accurate modeling of lumbar soft tissues is inadequate, and the general model fails to fully account for individual differences. Thus, it is of utmost importance to establish a model that precisely reflects individual characteristics. In the study of multifactor coupling, the simulation of complex loads is incomplete, and there is a lack of dynamic coupling between bone healing, tissue remodeling, and the mechanical behavior of screws. Regarding long-term performance evaluation, there is a deviation between the fatigue failure analysis and the actual situation, necessitating improvement by integrating clinical data. The design of new type screws requires optimization with the aid of finite element analysis to balance stability and mechanical performance. Although personalized screw design represents a trend, relevant research is scarce.

This study developed a refined finite element model of the lumbar spine and conducted finite element simulations in the lumbar segments and sacrum using a new patented medical device, transverse process-pedicle screw (TPPS) fixation system. A comprehensive 3D finite element model was proposed to analyze the changes in ROM, stress, displacement of the vertebrae, and TPPS pre- and post-surgery and confirm the effectiveness and safety of TPPS. This study would provide valuable insights into clinical surgeries and postoperative recovery of patients.

## Materials and methods

### Model acquisition

The lumbar CT images were obtained from a 23-year-old healthy male volunteer who was confirmed to have no lumbar-related diseases through clinical and radiological examinations using a 64-slice spiral CT scanner (GE Medical Systems, Chicago, IL, USA) in the First Affiliated Hospital of Jinan University (Guangzhou, Guangdong, China). The image data were processed using a workstation equipped with 12th Gen Intel Core i5-12400F processor at 2.50 GHz, 16.0 GB RAM, and Windows 11 (64 bit) operating system. All procedures of this study were approved by the Ethics Committee of Jinan University (Guangzhou, Guangdong, China). The written informed consent was obtained from the participant.

### Lumbar spine model construction

#### (1) Importing DICOM images and creating masks

The CT image data were imported into the medical modeling software, Mimics 21.0 (https://www.materialise.com/) in DICOM format. Mimics automatically generated tomographic images with default settings for scanning pixel size, resolution, and layer spacing. The threshold range of 96 – 2,941 was selected based on the bone density of the scanned subject. The CT slice interval was set as 0.5 mm. When scanning from L1 to L5, the upper limit of the scanning range included the lower edge of the T12 vertebral body, and the lower limit extended to the upper edge of the S1. The scanner angle was parallel to the scanning bed. However, when scanning intervertebral discs, the scanner angle was parallel to the centerline of the scanned intervertebral disc. oft tissue, The window width and level were set as 300 – 500 HU and 40 – 60 HU, respectively for soft tissue observation, and 1,000 – 1,500 HU and 250 – 350 HU, respectively for bone tissue observation. Processing coarse images in Mimics is a crucial step in 3D modeling because, when importing the DICOM files into Mimics, errors can occur, leading to insufficient accuracy in the 3D model. Each CT image layer was edited based on anatomical principles, refining the geometric shape to match a normal human lumbar spine. This process involved editing three views, erasing extraneous parts, and supplementing missing sections using the Edit Masks command. After the initial smoothing, the model was imported into Geomagic Wrap 2021 (3D Systems, Rock Hill, SC, USA) for further refinement. Based on anatomical principles, the vertebral model was smoothed and denoised to ensure it closely resembled a real human lumbar spine. The initial vertebral model was then extracted, contour lines modified, and surface patches constructed and repaired. The model was then gridded, the surface fitted, and the cortical bone solidified. Each vertebral body was then inwardly offset by 2 mm, polished to create cancellous bones, and intersecting surfaces and sharp areas were repaired. The finalized cortical and cancellous bone models were saved in STEP format.

#### (2) Model assembly

The vertebrae were assembled in SolidWorks (https://www.solidworks.com/zh-hans) to form the overall lumbar appearance. Details such as articular cartilage, nucleus pulposus, and endplates with the thickness setting at 0.5 mm were then added. Boolean operations were used to differentiate between cortical and cancellous bone. The finalized solid model was imported into ANSYS (https://www.ansys.com/) for ligament modeling. Once the ligaments were created, the entire lumbar spine model was complete. The postoperative lumbar spine lateral, anterior, and posterior views were shown in Figure 1.

The TPPS solid model was created in SolidWorks after initial 3D modeling. The TPPS model was

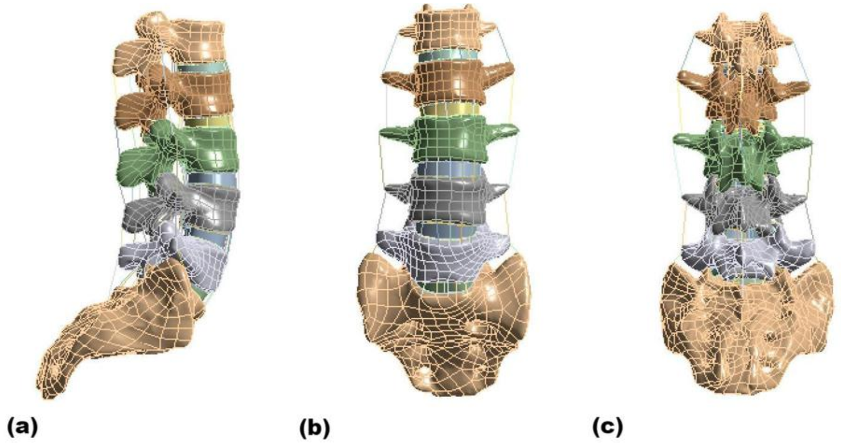

**Figure 1.** The normal lateral (a), anterior (b), and posterior (c) views of the lumbar spine.

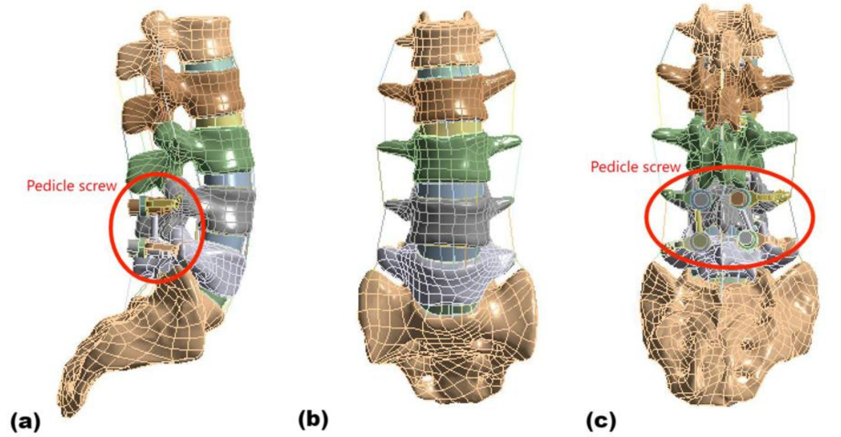

**Figure 2.** The lateral (a), anterior (b), and posterior (c) views of the lumbar spine after surgery.

imported into ANSYS for optimization, removing threads and interference areas according to finite element simplification principles to enhance computational efficiency without compromising accuracy. The TPPS model was coupled with the lumbar model in SolidWorks by implanting TPPS at L4 and L5 following clinical surgical methods with the steel plate adhered to the vertebral body using the surface command to simulate orthopedic surgery. The completed postoperative model was then exported in STEP format for final assembly in ANSYS. The dimensions of the transverse process plate could be adjusted during surgery with screw specifications set at 2.6 mm in diameter and 7 mm in length (Figure 2).

### (3) Contact setting and ligament addition

The model was imported into ANSYS for ligament modeling using line elements to simulate ligament structures. Different cross-sectional areas and elastic moduli were applied to simulate various ligaments set as tension-only rod elements during analysis. Contact tolerances were adjusted, and contact numbers and quality were verified before specific contact settings were applied. Contact between articular cartilage and vertebrae, ligaments and vertebrae, nucleus pulposus and annulus fibrosus, endplates and vertebrae, and endplates and annulus fibrosus were set as bonded with other contacts set as no separation.

### (4) Load and boundary conditions

In this study, the working conditions of the lumbar spine were simulated in the following specific ways. During flexion, the inferior surface of the sacrum was fixed, and an axial load of 300 N and a positive moment of 3.75 Nm about the x-axis were applied to the superior surface of the L1 vertebral body, resulting in the overall flexion of the lumbar spine with the sacrum fixed (Figure 3). During extension, the inferior surface of the sacrum was also fixed, and an axial load of 300 N and a negative moment of 3.75 Nm about the x-axis were applied to the superior surface of the L1 vertebral body, thereby causing the overall extension of the lumbar spine with the sacrum fixed. During bending, the inferior surface of the sacrum was fixed, and an axial load of 300 N and a negative moment of 3.75 Nm about the y-axis were applied to the superior surface of the L1 vertebral body, making the lumbar spine laterally bend as a whole with the sacrum fixed. During rotation, the inferior surface of the sacrum was fixed, and an axial load of 300 N and a negative moment of 3.75 Nm about the z-axis were applied to the superior surface of the L1 vertebral body, thus leading to the overall axial rotation of the lumbar spine with the sacrum fixed (Figure 3). These operations and the application of moments and loads aimed to deeply explore the mechanical performance and changes of the lumbar spine under different working conditions.

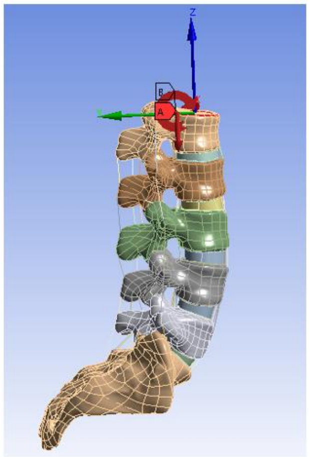

**Figure 3.** Boundary conditions for lumbar flexion.

### Validation of model effectiveness

Material properties such as Poisson's ratio and elastic modulus were assigned to each part of the model with specific cross-sectional areas set for ligaments. Hexahedral elements were used for mesh settings of the model with a mesh size of 0.5 mm for articular cartilage and adjustable mesh sizes from 0.5 mm to 2 mm for other parts based on simulation requirements. Finite element studies of the lumbar spine require comparative validation of the model. When simulating flexion, extension, right bending, and right rotation conditions, a 300 N axial load was applied to the upper surface of the L1 vertebral body to simulate body weight, and a 3.75 Nm torque was applied from different directions to simulate various lumbar spine activity conditions. The ROM of the model was compared with that of the reference models developed by other scientists to biomechanically valid proposed model for lumbar spine simulations under different conditions.

## Results and discussion

### Model material properties and comparative validation

Based on extensive literature review, suitable material properties for each part of the model were obtained and listed in Table 1. Further, the proposed model was compared to two reference models developed by Zhang *et al*. and Rohlmann *et al*., respectively [21, 22]. The results showed that the ROM of proposed model was similar to that of the reference models (Figure 4), indicating that the model was biomechanically valid and could be used for lumbar spine simulations under different conditions.

### Preoperative model intervertebral disc stress analysis

Under the flexion state, the peak stresses of L1/L2, L2/L3, L3/L4, L4/L5, L5/S1 intervertebral discs were 0.503, 0.558, 0.527, 0.929, 1.429 MPa, respectively, while, in the extension state, the peak stresses were 0.476, 0.581, 0.438, 0.919, 1.130 MPa, respectively, and during bending, the

**Table 1.** Material properties of each part of the model.

| Material | Young's modulus (MPa) | Poisson's ratio | Cross-section area (mm²) |
|---|---|---|---|
| Cortical bone | 12,000 | 0.3 | - |
| Cancellous bone | 100 | 0.3 | - |
| Endplate | 25 | 0.25 | - |
| Fibrous ring | 4.2 | 0.45 | - |
| Nucleus pulposus | 1 | 0.499 | - |
| Anterior longitudinal | 7.8 | 0.3 | 22.4 |
| Posterior longitudinal ligament | 10 | 0.3 | 7.0 |
| Ligamentum flavum | 15 | 0.3 | 14.1 |
| Capsular ligament | 7.8 | 0.3 | 10.5 |
| Interspinous ligament | 8 | 0.3 | 0.6 |
| Supraspinous ligament | 8 | 0.3 | 10.5 |
| Intertransverse ligament | 10 | 0.3 | 14.1 |
| TPPS | 110,000 | 0.3 | - |

peak stresses were 0.462, 0.547, 0.547, 0.649, 1.362 MPa, respectively, further, in axial rotation, the peak stresses were 0.397, 0.409, 0.323, 0.515, 1.640 MPa, respectively.

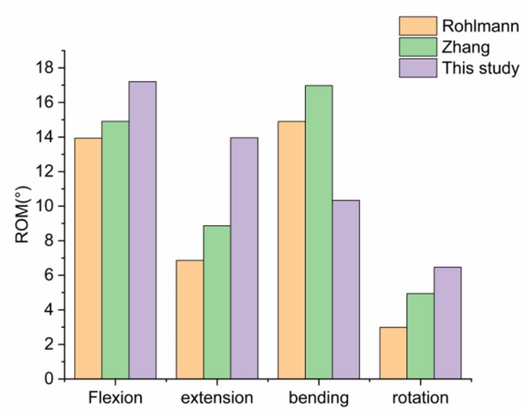

**Figure 4.** ROM comparison.

During preoperative lumbar flexion, stress was evenly distributed on the annulus fibrosus with the overall disc stress increasing from the L1/L2 disc downwards, but decreasing by 5.6% at the L3/L4 disc. At the L5/S1 disc, there was stress concentration at the posterior left side of the annulus fibrosus, and a trend of stress concentration at the posterior right side, though the stress was smaller than that on the left. The peak stress at L5/S1 during flexion was 1.428 MPa. During preoperative lumbar extension, the overall disc stress increased from top to bottom, but decreased by 24.7% at the L3/L4 disc. There was stress concentration at the posterior left side of the annulus fibrosus at L5/S1 with a peak stress of 1.1296 MPa. During preoperative right bending, stress was mainly concentrated on the right side of the disc with the nucleus pulposus under minimal stress and the stress primarily distributed around the annulus fibrosus. The stress on the disc increased from top to bottom with some stress concentration at the posterior side of the annulus fibrosus at L5/S1. The peak stress at L5/S1 during right bending was 1.3616 MPa. The left side of the disc was under tension while the right side was under compression, consistent with the actual stress distribution in the human lumbar spine. Comparison of flexion, extension, and right bending, the results showed that annulus fibrosus experienced the highest stress during right rotation, which was significantly higher than that in the nucleus pulposus. The overall disc stress increased from the L1/L2 disc downwards but decreased by 20.86% at the L3/L4 disc. There was some stress concentration at the posterior side of the annulus fibrosus at L5/S1 with a peak stress of 1.64 MPa during right rotation. Stress was concentrated on the left side of the annulus fibrosus during right rotation (Figure 5). The results suggested that, during the right bending, stress was concentrated

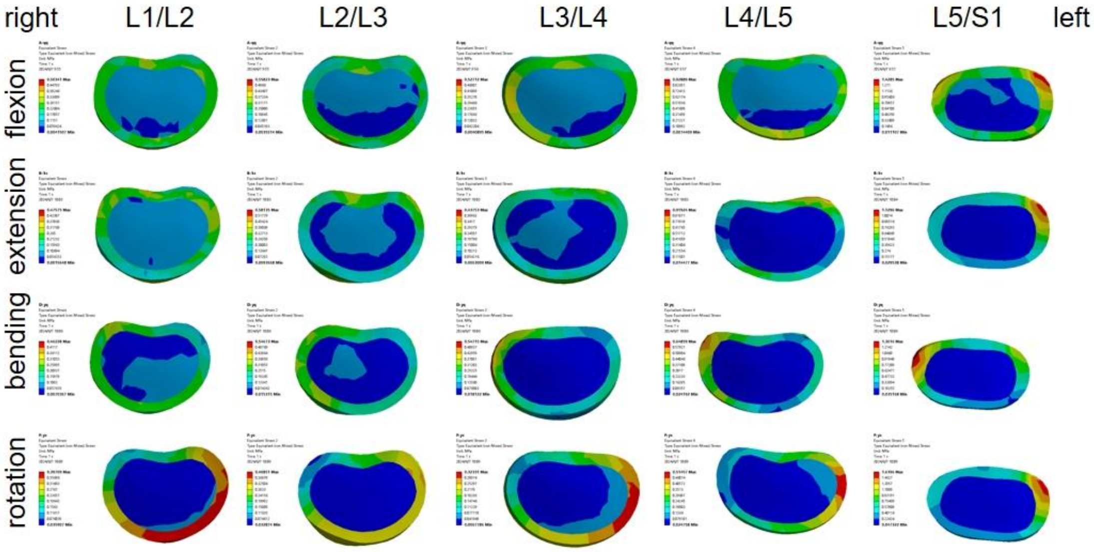

**Figure 5.** Preoperative stress cloud map of each intervertebral disc.

on the right side of the disc due to compression on the right side during the right bending. During right rotation, stress was concentrated on the left side of the annulus fibrosus with a smaller stress concentration area, resulting in the highest stress peak among all conditions. These stress trends indicated that the model accurately reflected the mechanical behavior of the lumbar spine under various conditions, making it suitable for biomechanical simulations.

### Postoperative model intervertebral disc stress analysis

The simulation results showed that, under the flexion state, the stresses of L1/L2, L2/L3, L3/L4, L4/L5, L5/S1 intervertebral discs were 0.647, 0.605, 0.554, 0.586, 1.279 MPa, while that of TPPS was 201.93 MPa. In the extension state, the stresses of L1/L2, L2/L3, L3/L4, L4/L5, L5/S1 were 0.6, 0.44, 0.444, 0.365, 1.117 MPa, while that of TPPS was 191.17 MPa. In the bending state, the stresses of L1/L2, L2/L3, L3/L4, L4/L5, L5/S1 were 0.52, 0.617, 0.533, 0.49, 1.036 MPa, while that of TPPS was 178 MPa. Under the rotation state, the stresses of L1/L2, L2/L3, L3/L4, L4/L5, L5/S1, and TPPS were 0.853, 0.493, 0.495, 0.49, 1.406, and 201.45 MPa, respectively. Under the same boundary conditions, after the TPPS implantation, the stress on the surgical segment L4/L5 disc significantly decreased and was relatively uniform with only the L5/S1 disc showing noticeable differences in distribution of stress between the annulus fibrosus and the nucleus pulposus during flexion. The stresses on the lumbar discs of L1/L2, L2/L3, L3/L4, L4/L5, and L5/S1 decreased by -28.5%, -8.37%, -5.1%, 36.9%, and 10.46%, respectively. Compared to the preoperative lumbar spine, the stress reduction was most significant at the surgical segment L4/L5 disc with a decrease of 36.9%. Compared to the normal lumbar spine stress cloud diagrams, the stress concentration range and peak stress on the L5/S1 disc after surgery were smaller with a reduction of 10.47%. Although the stress on the L5/S1 disc decreased, the reduction was smaller compared to that on the L4/L5 disc. During extension, the stresses on the lumbar discs L1/L2, L2/L3, L3/L4, L4/L5, and L5/S1 decreased by -26.1%, 24.3%, -1.5%, 60.3%, and 1.1%, respectively. Stress reduction was most significant at the L4/L5 disc with a decrease of 60.3%. Compared to the normal lumbar spine stress cloud diagrams, the stress concentration range and value on the L5/S1 disc after surgery were smaller than that in flexion conditions with a reduction of 1.1%. During right bending, the

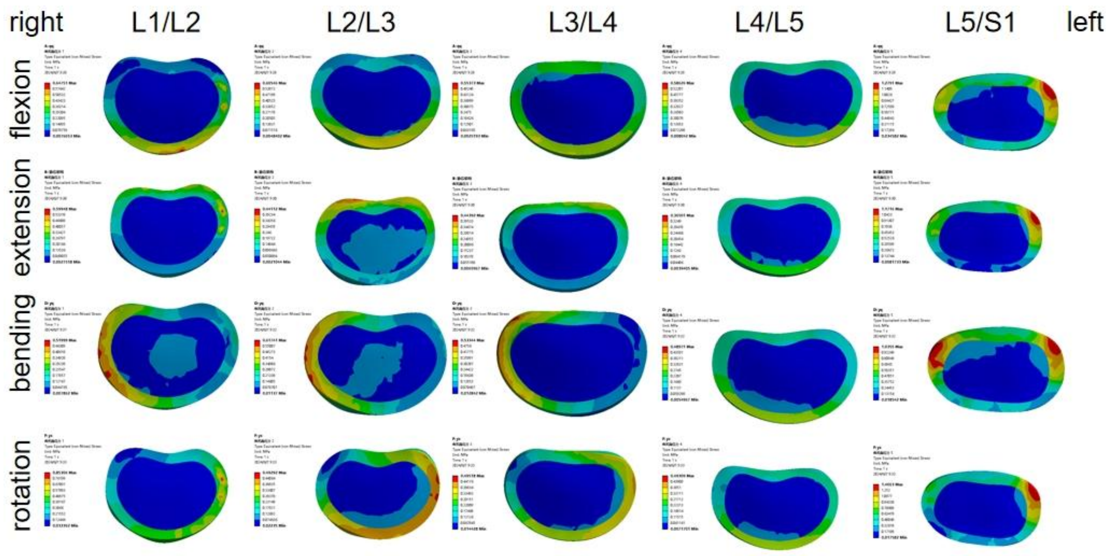

**Figure 6.** Postoperative stress cloud map of each intervertebral disc.

stresses on the lumbar discs L1/L2, L2/L3, L3/L4, L4/L5, and L5/S1 decreased by -12.5%, -12.9%, 2.6%, 24.5%, and 23.9%, respectively. The stress on the discs was concentrated on the right side of the annulus fibrosus with minimal stress on the nucleus pulposus and low stress on the left side of the annulus fibrosus. The stress reduction was most significant at the surgical segment L4/L5 disc. During right rotation, the stresses on all lumbar discs decreased by -114.8%, -20.7%, -53.1%, 4.8%, and 14.2% from L1 to S1, respectively. The peak stress on the lumbar intervertebral discs was the highest under various conditions with a noticeable difference in the stress distribution cloud map. The stress was concentrated on the annulus fibrosus, while the nucleus pulposus was basically unstressed. The stress on the intervertebral discs increased progressively from top to bottom. Compared to the preoperative lumbar spine, the postoperative lumbar spine showed an increase in stress on L1/L2, L2/L3, and L3/L4 intervertebral discs under right rotation, while the stress on the L4/L5 segment decreased by 4.8%. The reduction in stress on L5/S1 disc was greater than that in the corrected L4/L5 segment (Figure 6). After the implantation of TPPS, the stress on the intervertebral discs during lumbar flexion decreased, and the overall ROM of the lumbar spine in daily activities was significantly reduced, which indicated that TPPS provided excellent stability to the lumbar spine. During flexion, the stresses on L1/L2, L2/L3, and L3/L4 intervertebral discs increased, while the stress on the surgical segment L4/L5 decreased, and the stress on the lower L5/S1 disc also decreased. There was stress concentration in the lateral posterior part of the annulus fibrosus, but compared to pre-operation, the stress concentration range was reduced and the stress decreased, although the decrease was not as significant as in L4/L5 segment. Therefore, lumbar spine correction surgery could reduce the pressure on L4/L5 segment. Except for L5/S1 disc, the stress on other non-surgical segments increased during activities under the same boundary conditions of post-operation. When the lumbar spine extended in post-operation conditions, the stresses on L1/L2 and L3/L4 discs increased, while the stresses on the other segment discs decreased. The stress on L5/S1 disc decreased but the reduction was less significant compared to the surgical segment L4/L5. Although the stress on the intervertebral discs decreased during the extension after the corrective surgery, it was important to note that the stresses on other segments, excluding the surgical and adjacent segments, were higher than that before. Therefore, patients should avoid large scale activities post-surgery to prevent secondary injuries. During lateral bending to the right after the surgery, the stress reduction on L4/L5 and L5/S1 discs was similar. The stress on L3/L4 disc decreased, and the stress concentration range on L5/S1 disc reduced along with the stress itself, which suggested that TPPS effectively reduced disc stress post-correction surgery, showing good surgical outcomes for conditions like lumbar disc protrusion and lumbar disc bulging. During the right rotation after the operation, the stress on L5/S1 disc significantly decreased, and the stress concentration range became smaller. However, the stresses on L1/L2, L2/L3, and L3/L4 discs increased during activity, which indicated that the correction surgery fixed the L4 and L5 vertebrae, resulting in stress compensation at L1/L2, L2/L3, and L3/L4 discs. Hence, patients should avoid large scale lumbar movements, especially twisting motions, after the surgery as this could place greater stress on the vertebrae coupled with the screws and rods, potentially causing vertebral fractures.

**Preoperative model analysis of intervertebral disc displacement**

The results showed that, under the flexion state, the displacement of intervertebral discs at L1/L2, L2/L3, L3/L4, L4/L5, and L5/S1 reached 35.021 mm, 25.024 mm, 15.697 mm, 7.2862 mm, and 1.9617 mm, respectively. In the extension state, the displacement of L1/L2, L2/L3, L3/L4, L4/L5, L5/S1 were 22.135 mm, 13.842 mm, 6.7838 mm, 2.1524 mm, 0.7362 mm, respectively. During the bending state, the displacement of L1/L2, L2/L3, L3/L4, L4/L5, L5/S1 were 16.575 mm, 11.716 mm, 7.7351 mm, 4.2992 mm, 1.6285 mm, respectively. In axial rotation, the displacement of L1/L2,L2/L3, L3/L4, L4/L5, L5/S1 were 13.165 mm, 10.733 mm, 7.7909 mm, 4.4254 mm, 1.5 mm, respectively. During flexion, displacement was primarily concentrated at the anterior end of the disc with smaller displacements at the posterior end. The overall disc displacement decreased from L1/L2 disc downwards with a peak displacement of 35 mm at L1/L2. The peak displacement of each lumbar disc decreased by 28.5%, 37.3%, 53.6%, and 73.1%, respectively, compared to the previous disc. In normal lumbar flexion, the displacement of each disc decreased progressively with a diminishing reduction for each subsequent disc. During extension, the deformation of the upper discs was still at the anterior end, but the peak deformation gradually moved towards the posterior end of the discs from top to bottom. The overall disc displacement decreased from L1/L2 disc downwards with a peak displacement of 22.14 mm at L1/L2. The peak displacement of each lumbar disc decreased by 42%, 47%, 68%, and 66%, respectively, compared to the previous disc. The displacement patterns were similar to those during flexion but with smaller values. During extension, the peak displacement of L5/S1 disc was on the left side, corresponding to the stress concentration observed in the stress cloud diagrams consistent with actual mechanical conditions. During the right bending, the maximum disc deformation was primarily concentrated on the right side. The overall disc displacement decreased from L1/L2 disc downwards with a peak displacement of 16.575 mm at L1/L2. The peak displacement of each lumbar disc decreased by 44.76%, 34%, 44.4%, and 62.1%, respectively, compared to the previous disc. In the normal lumbar right bending, the displacement of each disc decreased progressively. However, the reduction at L3/L4 compared to L2/L3 was smaller than the reduction at L2/L3 compared to L1/L2, which indicated that different lumbar discs exhibited different displacement effects during different activities, highlighting the necessity of lumbar modeling for different patients. During the right bending, the peak displacement of L5/S1 disc was on the right side, corresponding to the stress concentration observed in the stress cloud diagrams, and consistent with mechanical principles. During the right rotation, the displacement of the upper discs was concentrated on the left side with the rotation trend becoming more pronounced downwards. The overall disc displacement decreased from L1/L2 disc downwards with a peak displacement of 13.165 mm at L1/L2. The peak displacement of

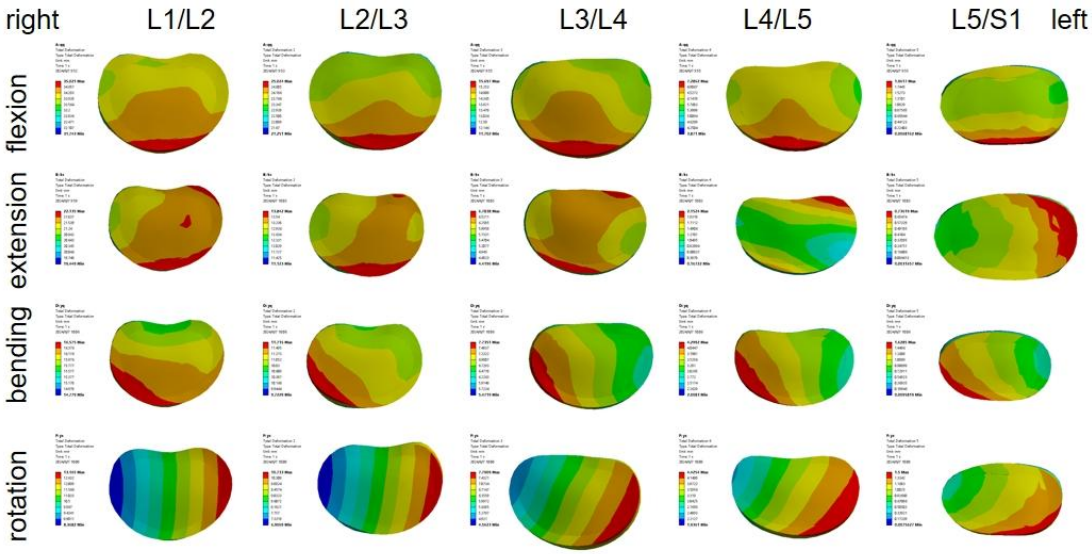

**Figure 7.** Preoperative Displacement cloud map of each intervertebral disc.

each lumbar disc decreased by 18.47%, 27.4%, 43.2%, and 66.1%, respectively, compared to the previous disc. The displacement patterns were similar to those during flexion and extension but with smaller values. During the right rotation, the displacement of disc was smaller than the previous conditions, but the rotation trend was more pronounced. The peak displacement of L5/S1 disc was on the left side, corresponding to the stress concentration observed in the stress cloud diagrams, and consistent with mechanical principles. The displacement cloud diagrams demonstrated that, when considering only disc displacement, there was no obvious boundary between the nucleus pulposus and the annulus fibrosus, indicating that the displacement results were not significantly related to material properties (Figure 7).

### Postoperative model analysis of intervertebral disc displacement

The results showed that, under the flexion state, the displacements of L1/L2, L2/L3, L3/L4, L4/L5, L5/S1 intervertebral discs were 14.052 mm, 10.131 mm, 6.761 mm, 3.861 mm, 1.593 mm, and that of TPPS was 4.887 mm. In the extension state, the displacements of L1/L2, L2/L3, L3/L4, L4/L5, L5/S1, and TPPS were 3.53 mm, 2.526 mm, 2.173 mm, 1.629 mm, 0.982 mm, and 1.614 mm, respectively. During the bending state, the displacements of L1/L2, L2/L3, L3/L4, L4/L5, L5/S1, and TPPS were 9.156 mm, 6.678 mm, 4.729 mm, 2.85 mm, 1.305 mm, and 3.246 mm. Under the rotation state, the displacements of L1/L2, L2/L3, L3/L4, L4/L5, L5/S1, and TPPS were 8.488 mm, 6.838 mm, 4.901 mm, 2.856 mm, 1.35 mm, and 3.678 mm, respectively. During forward flexion, the displacements of lumbar intervertebral discs from L1/L2 to L5/S1 decreased by 59.9%, 59.5%, 56.9%, 47%, and 18.8%, respectively. The displacement still concentrated on the anterior part of the discs while maximum displacement values decreased compared to pre-surgery. Overall displacement trends remained unchanged with the nucleus pulposus and annulus fibrosus showing continuous reduction from top to bottom of the discs post-surgery. Significant reduction in displacement was observed particularly in the L1/L2, L2/L3, and L3/L4 discs. During extension, the displacement from L1/L2 to L5/S1 decreased by 84.1%, 81.8%, 68%, 24.3%, and -33.4%, respectively. Displacement concentrated at the posterior end of the lumbar discs with discernible differences between the nucleus pulposus and annulus fibrosus. Peak displacement values gradually decreased from top to bottom and shifted towards the lateral aspects of the discs.

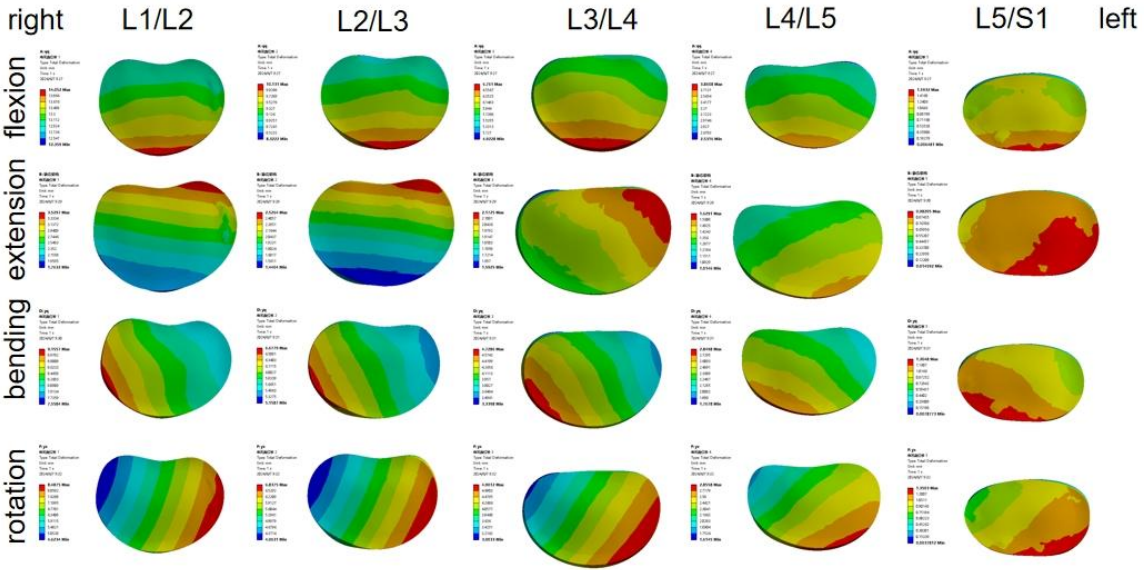

**Figure 8.** Postoperative cloud map of displacement of intervertebral discs.

L1/L2 and L2/L3 discs exhibited the most pronounced reduction in displacement post-surgery with the segment at L4/L5 showing less reduction compared to the first two discs. During the right lateral bending, the displacement from L1/L2 to L5/S1 decreased by 44.8%, 43%, 38.9%, 33.7%, and 19.9%, respectively. The displacement peaked towards the right end, decreasing towards the left with minimal displacement at the farthest left end. Displacement reduction during the right lateral bending was more uniform compared to forward flexion and extension, likely due to the symmetrical nature of TPPS affecting disc displacement less during lumbar lateral bending. During right rotation, the displacement from L1/L2 to L5/S1 decreased by 35.5%, 36.3%, 37.1%, 35.5%, and 10%, respectively. Displacement concentrated at the left end of the discs with clear layering of the first four discs and distinct patterns observed in the displacement cloud map. Postoperative disc displacement decreased compared to that of pre-surgery with right rotation showing less reduction in disc displacement compared to forward flexion, extension, and right lateral bending (Figure 8). The results indicated that TPPS had the greatest impact on intervertebral disc displacement during forward flexion and extension after the correction surgery with less influence during lateral bending and minimal impact during axial rotation. However, TPPS still exerted a limiting effect on disc displacement under various conditions.

### Postoperative model cortical bone stress analysis

Under the flexion state, the maximum cortical bone stress was 60 MPa, while, in the extension state, the maximum cortical bone stress was 45.4 MPa. During the bending state, the maximum cortical bone stress was 54.89 MPa and, under the rotation state, the maximum cortical bone stress was 53.6 MPa. After the TPPS implantation, stress on the cortical bone during daily lumbar activities on post-simulation of corrective surgery was the highest at the L4 vertebra. Stress concentration primarily occurred at the screw coupling points with higher stress observed at the distal end of the left transverse process. Under all conditions, maximum stress occurred during forward flexion, reaching 60 MPa, which was far below the ultimate stress limit of human bone (182 MPa) [23], indicating the safety of TPPS implantation in humans (Figure 9).

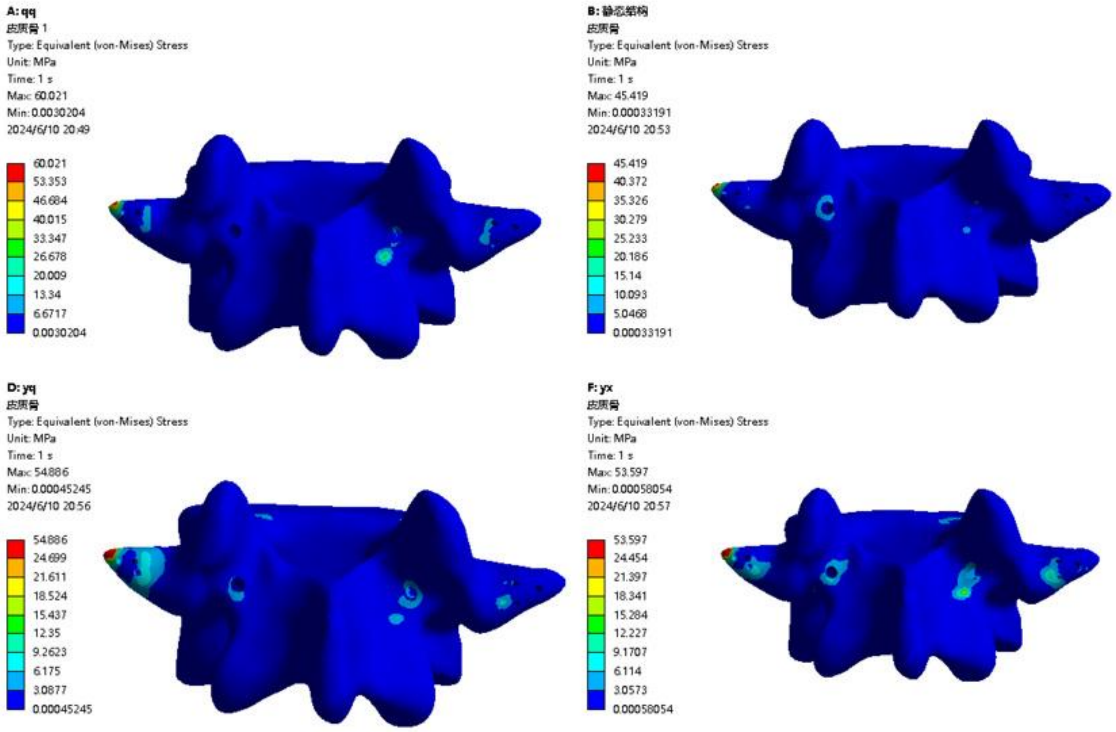

**Figure 9.** Postoperative lumbar cortical bone stress cloud map.

**Postoperative model screw stress and displacement analysis**

The results demonstrated that, under the flexion state, the maximum displacement of TPPS was 4.887 mm, and the maximum stress of TPPS was 201.93 MPa. In the extension state, the maximum displacement and stress of TPPS were 1.614 mm and 191.17 MPa. During the bending state, the maximum displacement of TPPS was 3.246 mm and the maximum stress was 178 MPa. Under the rotation state, the maximum displacement of TPPS was 3.678 mm and the maximum stress was 201.45 MPa. It was evident that the maximum displacement of TPPS occurred during forward flexion, reaching 4.887 mm with the highest stress also occurring during lumbar forward flexion, reaching 201.93 MPa. During forward flexion, the maximum TPPS displacement was concentrated at the tail end of the screws, whereas during extension, it was concentrated on the transverse process plate. The right lateral bending exhibited peak displacement at both the transverse process plate and the tail end of the screws, while right rotation primarily concentrated displacement at the transverse process plate (Figure 10). According to the stress cloud map of the transverse steel plate, the stress on the TPPS under various conditions mainly concentrated at the connecting rod and transverse process plate. Surgeons should tailor the TPPS transverse process plate based on the patient's lumbar physiological curvature and adjust the coupling position and angle between the plate and the lumbar spine. According to the simulation results, the sharp parts of the transverse process plate could be modified to rounded corners to minimize or avoid stress concentration at the plate.

## Conclusion

TPPS effectively reduced stress on diseased segment intervertebral discs following corrective surgery, providing overall stability to the lumbar spine. It has shown positive surgical outcomes for conditions such as lumbar disc herniation and

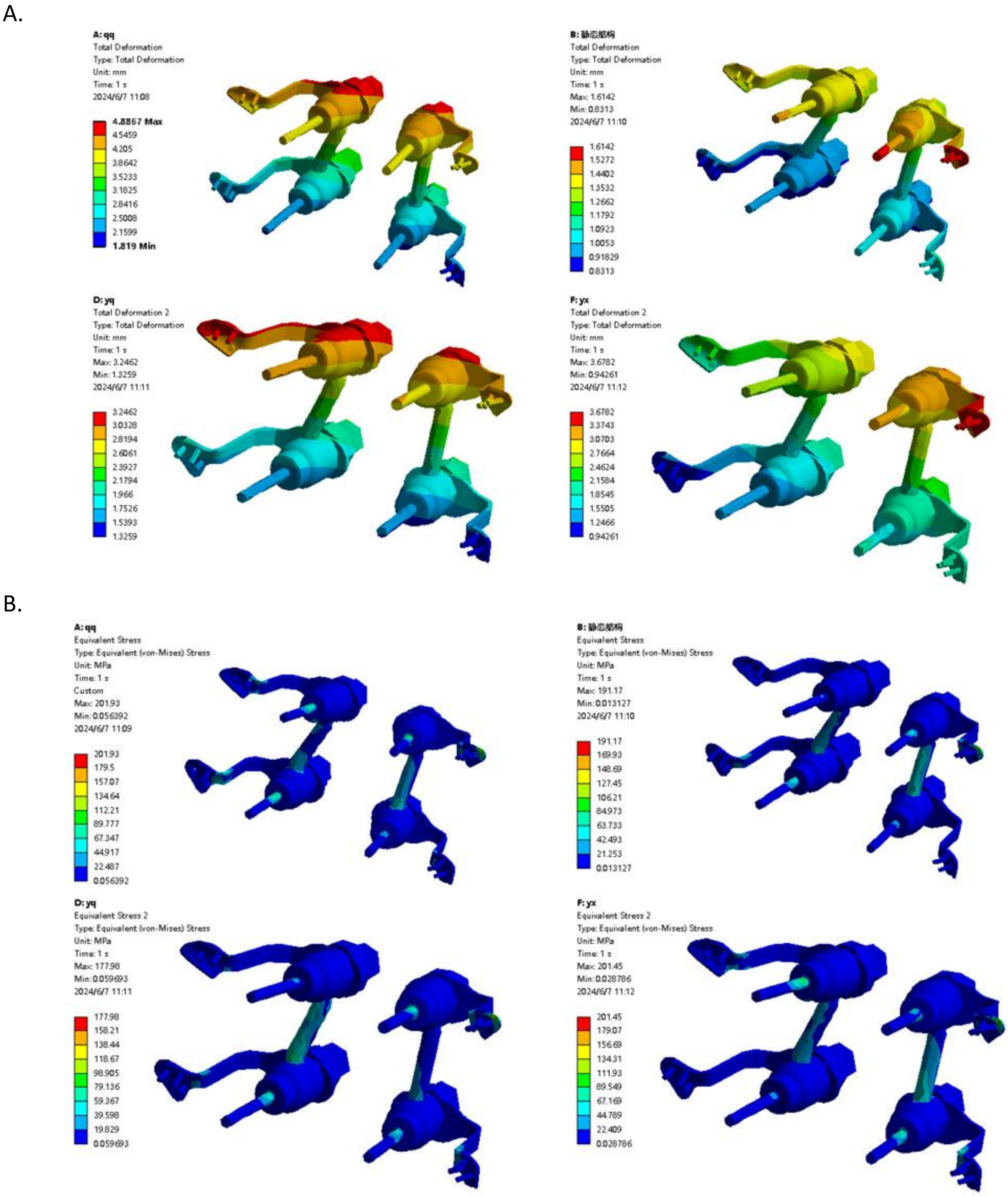

**Figure 10.** The displacement (A) and stress (B) cloud maps of TPPS.

bulging. Post-operation patients should limit lumbar activities and avoid twisting motions during rehabilitation to prevent additional stress on other lumbar disc segments, which could accelerate degeneration. Surgeons should customize TPPS transverse process plates based on the patient's lumbar curvature, adjusting the plate's position and angle to match the spine. According to the simulation results of this study, rounding the sharp edges of the transverse process plate could help minimize stress concentration and potential issues at the plate.

## References

1. Ala-kokko L. 2002. Genetic risk factors for lumbar disc disease. Ann Med. 34(1):42-47.
2. Fan W, Zhang C, Zhang DX, Gao LX, Zhang M. 2023. Biomechanical responses of the human lumbar spine to vertical whole-body vibration in normal and osteoporotic conditions. Clin Biomech. 102:105872.
3. Hussein M, Abdeldayem A, Mattar MM. 2014. Surgical technique and effectiveness of microendoscopic discectomy for large uncontained lumbar disc herniations: A prospective, randomized, controlled study with 8 years of follow-up. Eur Spine J. 23(9):1992-1999.
4. Li R, Shao X, Li X, Liu Y, Jiang W. 2021. Comparison of clinical outcomes and spino-pelvic sagittal balance in degenerative lumbar spondylolisthesis: Minimally invasive oblique lumbar interbody fusion (OLIF) versus transforaminal lumbar interbody fusion (TLIF). Medicine. 100(3):e23783.
5. Liu J, Gong X, Wang K, Li X, Zhang X, Sun J, *et al*. 2023. A comparison of the biomechanical properties of three different lumbar internal fixation methods in the treatment of lumbosacral spinal tuberculosis: Finite element analysis. Sci Rep. 13(1):11354.
6. Tang YC, Peng JC, Guo HZ, Zhen CG, Huang HS, Ma YH, *et al*. 2022. Comparison of pedicle screw fixation with or without cement augmentation combined with single-segment isthmic spondylolisthesis in osteoporotic spine. Sci Rep. 13:827.
7. Zhang L, Yang W, Ding G, Li P, Xiao Z, Chen Y, *et al*. 2025. Dispersion effect of bone cement after vertebroplasty using individualized unilateral external pedicle approach and bilateral pedicle approach. Chinese J Tissue Eng Res. 29(4):800.
8. Holland I. 1974. Fundamentals of the finite element method. Comput Struct. 4(1):3-15.
9. Welch-Phillips A, Gibbons D, Ahern DP, Butler JS. 2020. What is finite element analysis? Clin Spine Surg. 33(8):323-324.
10. Khuyagbaatar B, Kim K, Kim YH. 2024. Recent developments in finite element analysis of the lumbar spine. Int J Precis Eng Manuf. 25(2):487-496.
11. Cao L, Liu Y, Mei W, Xu J, Zhan S. 2020. Biomechanical changes of degenerated adjacent segment and intact lumbar spine after lumbosacral topping-off surgery: A three-dimensional finite element analysis. BMC Musculoskelet Disord. 21:1-7.
12. Sengul E, Ozmen R, Yaman ME, Demir T. 2021. Influence of posterior pedicle screw fixation at L4–L5 level on biomechanics of the lumbar spine with and without fusion: a finite element method. Biomed Eng Online. 20:1-19.
13. Imai K. 2015. Computed tomography-based finite element analysis to assess fracture risk and osteoporosis treatment World J Exp Med. 5(3):182.
14. Zhang Q, Chon T, Zhang Y, Baker JS, Gu Y. 2021. Finite element analysis of the lumbar spine in adolescent idiopathic scoliosis subjected to different loads. Comput Biol Med. 136:104745.
15. Cai XY, Sun MS, Huang YP, Liu ZX, Liu CJ, Du CF, *et al*. 2020. Biomechanical effect of L4–L5 intervertebral disc degeneration on the lower lumbar spine: A finite element study. Orthop Surg. 12(3):917-930.
16. Yamamoto I, Panjabi MM, Crisco T, Oxland T. 1989. Three-dimensional movements of the whole lumbar spine and lumbosacral joint. Spine, 14(11):1256-1260.
17. Shirazi-Adl A. 1994. Analysis of role of bone compliance on mechanics of a lumbar motion segment, J Biomech Eng. 116(4):408-412.
18. Kiapour A, Goel V. 2009. Biomechanics of a novel lumbar total motion segment preservation system: A computational and *in vitro* study. Bonezone. 8:86-90.
19. Kiapour A, Anderson DG, Spenciner DB, Ferrara L, Goel VK. 2012. Kinematic effects of a pedicle-lengthening osteotomy for the treatment of lumbar spinal stenosis. J Neurosurg Spine. 17(4):314-320.
20. Lin HM, Pan YN, Liu CL, Huang LY, Huang CH, Chen CS. 2013. Biomechanical comparison of the K-ROD and Dynesys dynamic spinal fixator systems–a finite element analysis. Biomed Mater Eng. 23(6):495-505.
21. Zhang Q, Zhang Y, Chon TE, Baker JS, Gu Y. 2023. Analysis of stress and stabilization in adolescent with osteoporotic idiopathic scoliosis: Finite element method. Comput Methods Biomech Biomed Engin. 26(1):12-24.
22. Rohlmann A, Neller S, Bergmann G, Graichen F, Claes L, Wilke HJ. 2001. Effect of an internal fixator and a bone graft on intersegmental spinal motion and intradiscal pressure in the adjacent regions. Eur Spine J. 10:301-308.
23. Chen J, Li J, Xin H. 1999. An investigation of mechanical properties of human bone. Journal of Jinan University Natural Science and Medicine Edition. 20:74-78.